Deformation Behavior of the Percolating Eutectic Intermetallic in HPDC and Squeeze-Cast Mg Alloys

BAO ZHANG,[1,5] KUN V. YANG,[2] ANUMALASETTY V. NAGASEKHAR,[1,4] CARLOS H. CÁCERES,[1,6] and MARK EASTON[3]

1.—Materials Engineering, School of Engineering, The University of Queensland, Brisbane, QLD 4072, Australia. 2.—Department of Materials Engineering, Monash University, Melbourne, VIC 3800, Australia. 3.—School of Aerospace, Mechanical and Manufacturing Engineering, RMIT University, Melbourne, VIC 3063, Australia. 4.—*Present address:* Carpenter Technology Corporation, PO Box 14662Reading, PA, USA. 5.—e-mail: ba.zhang.cn@gmail.com. 6.—e-mail: c.caceres@uq.edu.au

The structural compliance of the spatially interconnected intermetallic network in a squeeze-cast MRI230D alloy was determined using focused ion beam (FIB) data and finite element (FE) modeling, and compared with data for a high-pressure die-cast AZ91D and three binary Mg-RE alloys from the existing literature. The respective elastic responses were sorted out into two characteristic behaviors: for eutectic volume fractions less than ~22% the behavior was akin to that of highly compliant, bending-dominated structures, whereas for larger fractions, it reproduced that of structurally efficient, stretch-dominated microtruss structures. In all cases, the contribution from the interconnected network added to the total strength of the alloy an amount comparable with the strengthening expected from a similar volume fraction of dispersed particles. Being more compliant, the bending-dominated structures appeared less prone to developing damage by cracking at low strains than the stretch dominated ones.

INTRODUCTION

A number of authors have concluded that the profuse interconnection of the intergranular percolating intermetallic/eutectic phases evident in two-dimensional (2D) scanning electron microscopy (SEM) images of high-pressure die cast (HPDC) Mg-Al and Mg-RE* alloys should be considered as an additional strengthening mechanism.[1–4] Comprehensive morphological characterization of the percolating phases, obtained through focused ion beam (FIB) three-dimensional (3D) tomography, of the intermetallic phase in AZ91D[5] and of the eutectics in Mg-Nd, Mg-La, and Mg-Ce alloys,[6] combined with finite-element (FE) modeling[6–8] supported those assertions. Recent short anneal experiments[6] aimed at breaking up the spatial interconnection on HPDC Mg-Ce and Mg-La alloys showed that the 3D networks accounted for as much as between 20 MPa and 40 MPa of the alloy's strengths, or over 20% of their total strength, in close agreement with the numerical modeling. The modeling also showed that for a low volume fraction, the degree of interconnection is reduced making the interconnected phases more compliant, hence less prone to compromise the alloy's ductility. For large volume fractions of eutectic, the reinforcement is more efficient due to the increased interconnectivity but at the cost of early cracking of the interconnected branches.

In the current work, newly acquired data for a squeeze-cast MRI230 are used to model the elastic deformation behavior of the alloy's 3D interconnected eutectic network and to estimate its reinforcing effects on the alloys overall strength. The results are subsequently compared with the available data[6–8] for HPDC alloys AZ91D, Mg-La, Mg-Ce, and Mg-Nd. The set of alloys selected for comparison represent extreme cases in terms of volume fraction of the percolating intermetallic/eutectic, from relatively low (5.9%) for AZ91 to relatively high (30%) for the Mg-La alloys, whereas the inclusion of the squeeze-cast alloy aimed at showing that a similar type of interconnected microstructure, hence

---

*RE denotes a Ce-rich misch-metal containing 51.7 mass% Ce, 23.1 mass% La, 18.6 mass% Nd, and 6.5 mass% Pr.

Table I. Compositions and percolating phases of the alloys studied

Alloy	Casting process	Composition	Intergranular[a] Percolating Phase/s	References
AZ91D	High-pressure die cast	9 mass% Al 1 mass% Zn	Intermetallic $Mg_{17}Al_{12}$	5,8–10
Binary Mg-La		3.44 mass% La	Eutectic $Mg-Mg_{12}La$	4,6,7,11
Binary Mg-Ce		2.87 mass% Ce	Eutectic $Mg-Mg_{12}Ce$	
Binary Mg-Nd		3.53 mass% Nd	Eutectic $Mg-Mg_3Nd$	
MRI230D	Squeeze cast	6.8 mass% Al 1.91 mass% Ca	Eutectic $Mg-Al_2Ca$	3,12 this work.

[a]The relative coarseness of the divorced AZ91 alloy's eutectic allowed the detection of the eutectic intermetallic separate from the eutectic α-Mg in the FIB sectioning. For the other alloys, the whole eutectic was considered as the percolating phase. See Ref. 7 for further details.

Table II. Parameters of the FIB Tomography

Source	Voltage	Current	Resolution	Slice thickness	Number of slices
Ga^+ ions	30 kV	1.0 nA	1024×884	0.25 μm for AZ91D 0.2 μm for the remaining alloys	100

Further details can be found in Ref. 5.

exhibiting similar behavior, can be expected even when the solidification rate is not as extreme as in the HPDC process. The overall goals of the work were: (I) to show that squeeze-cast alloys exhibit the same type of interconnected network and (II) that predicting the effects of any 3D percolating intermetallic/eutectic network on both the strength and the ductility of Mg cast alloys is possible using a straightforward parameter, the volume fraction of eutectic.

MATERIALS AND DATA FOR ANALYSIS

Alloys

Table I lists the alloys' respective chemical compositions (obtained by Inductively coupled plasma atomic emission spectroscopy (ICP-AES)) and the relevant percolating phases.

3D FIB Sectioning and Reconstruction

For all alloys, a volume adjacent to the casting's surface was serially sectioned on a dual-beam FIB machine and SEM secondary electron images collected after each slice was removed. The images were subsequently aligned and subjected to sequential segmentation and reconstruction to obtain the respective 3D microstructures. Table II lists the relevant FIB parameters.

The squeeze-cast alloy specimen was obtained from a 7-mm-thick plate. With reference to Fig. 1, the sectioning was carried out normal to the plate surface, i.e., along the Y-direction. For the HPDC alloys, the selected volume represented the casting's

surface layer, or skin, whereas for alloy AZ91 a similar volume at the center of the casting's cross section, or core, was also studied. Further details for the HPDC alloys can be found in Refs. 6–8.

Numerical Modeling

The meshing of the 3D eutectic network was carried out with four-node tetrahedral elements (C3D4) using built-in tools from the commercial package Amira (version 5.3; FEI Company, Burlington, MA). The deformation behavior was subsequently modeled using the package ABAQUS (version 6.10).

For modeling, brittle fracture of the eutectic intermetallic phases was assumed to occur at a tensile strain of 0.7%. It was also assumed that plastic relaxation of pileup stresses on the Mg alloy matrix started at 0.7% plastic strain.**

Doing so imposed a lower bound for the (local) stress/strain because of the onset of damage on the interconnected branches orientated to take a load larger than average and an upper bound to the stress taken by the matrix. The simulations were limited to a maximum uniform (elastic + plastic) tensile strain of 1% in keeping with experiments that indicate that unidirectionally solidified eutectic composites fail in tension at a that strain value.[13,14] The space-filling matrix was ignored in the modeling

---

**In more practical terms, the modeling assumes that the eutectic intermetallic constrains the eutectic α-Mg in such a way that both composite's components remain elastic until the intermetallic cracks at 0.7% strain.
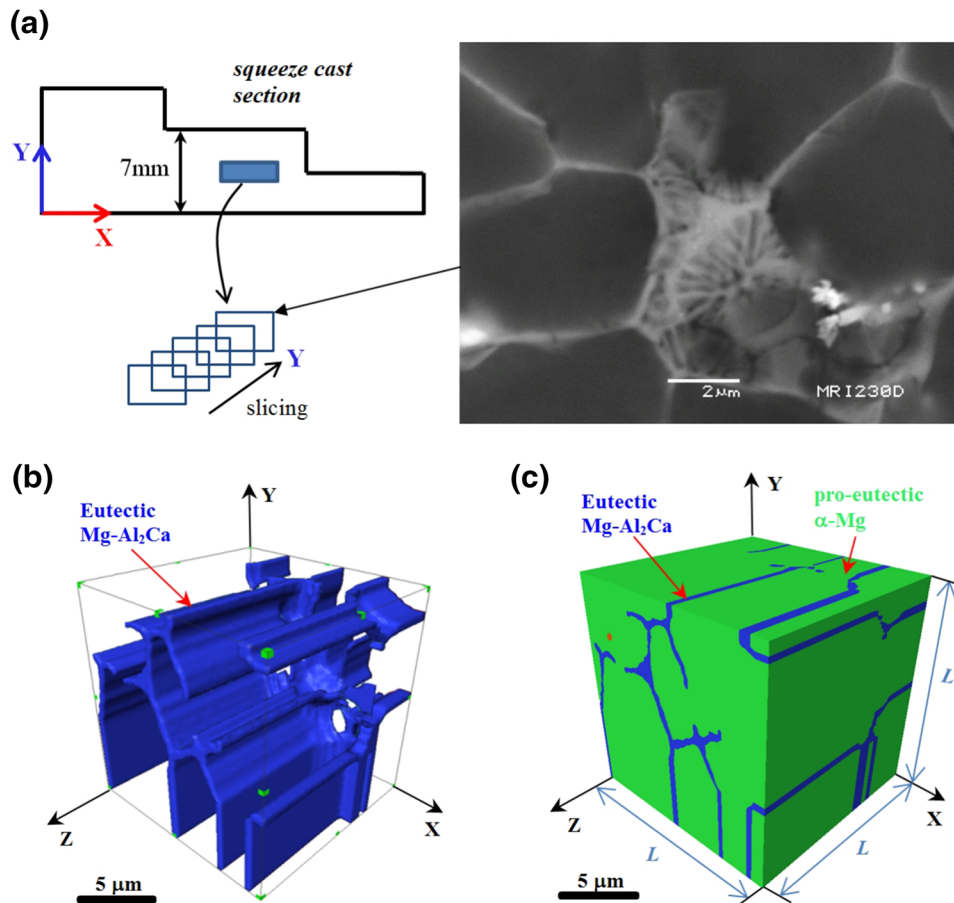
(a)

(b)

(c)

Fig. 1. (a) Representative SEM image of a section from the center of 7-mm-thick squeeze-cast MRI230D plate. (The *Y*-axis indicates the casting thickness direction.) (b) 3D microstructure of the percolating eutectic Mg-CaAl$_2$. (c) Cubic volume of the squeeze-cast MRI230D examined using FIB.

of all alloys. A more detailed justification of the model's basic assumptions can be found in Ref. 8.

3D Characterization

The volume fraction of the percolating phase within the sampled volume, denoted by f_p, was determined using the built-in tools of the Amira software.[15] The respective volume fractions of eutectic α-Mg and the intermetallic CaAl$_2$ that comprise the whole eutectic, denoted respectively by f^α and f^i, were calculated as per the liquid projection of the Mg-Al-Ca ternary system.[16] The volume fraction of the intermetallic within the sampled volumes is given by $(f_p \times f^i)$.

RESULTS

3D Reconstruction

Figure 1a shows a representative SEM image of the slice located at the center of 7-mm-thick MRI230D plate. The dark and light regions represent, respectively, the α-Mg and eutectic Mg-CaAl$_2$ phases. The reconstructed eutectic is shown in Fig. 1b. The complete sampled volume is shown in Fig. 1c, where the lighter (green) and darker (blue) zones represent the proeutectic α-Mg and the eutectic Mg-CaAl$_2$, respectively. The structure exhibits some
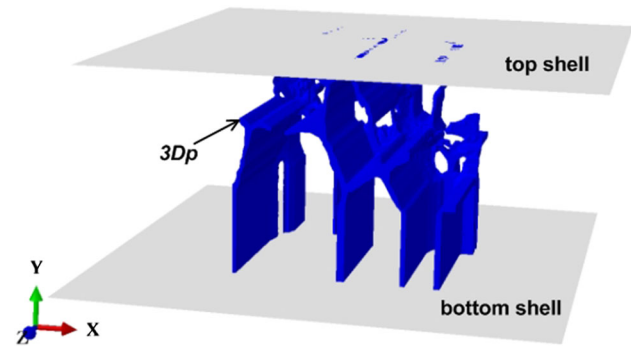

Fig. 2. FE model setup for alloy MRI230D.

directionality across the plate thickness consistent with the expected directions of heat extraction. The testing direction for the simulations was chosen across the solidification direction, as described below.

FE Modeling

The configuration of the FE model is illustrated by Fig. 2, where the eutectic Mg-CaAl$_2$ network was bounded by two rigid shells. A force F applied perpendicularly to the top shell results in a displacement δ parallel to the Y-axis. The average stress σ

and strain ε experienced by the 3D network, and its effective elastic modulus E_{3Dp} are given by:

$$\varepsilon = \ln(1 + \delta/L), \qquad (1)$$

$$\sigma = (1 + \delta/L) * F/L^2 \qquad (2)$$

$$E_{3Dp} = \sigma/\varepsilon \qquad (3)$$

Four-node tetrahedral elements (C3D4)[17] were used to discretize the spatial network. The element size was ~0.25 μm, in keeping with the prior studies of the alloys of Table I and to maintain consistency in the computed results.

Figure 3 shows the distributions of local strains at an applied uniform strain of 1%. The black regions indicate where cracking of the microtrusses and plastic relaxation of the matrix are expected to occur first. The elastic response of the reconstructed structure is described in the next section jointly with the other alloys.

DISCUSSION

Deformation Behavior

Table III lists the relevant microstructural parameters for the alloys selected for comparison, sorted to make evident the range of f_p-values, which varies between about 6% and 30%.

Figure 4[†] compares the modulus of the intermetallic ($Mg_{17}Al_{12}$) of AZ91D alloy and those of the whole eutectic for the rest of the alloys, determined assuming that the intermetallic reinforces the whole eutectic as long fibers do in a metal matrix composite:

$$E_p = f^i E_i + f^\alpha E_\alpha \qquad (4)$$

where E_i and E_α represent, respectively, the moduli of the eutectic intermetallic and α-Mg.

In the early stage of deformation, i.e., prior to 0.7% strain, the intermetallic (alloy AZ91D) or the whole eutectics (for the other alloys) deform elastically.[18] Past the strain of 0.7% (indicated by primed symbols), cracking of the intermetallic leads to $E_i' = 0$, whereas plastic deformation of the eutectic α-Mg implies a "plastic modulus" $E_\alpha' = 1.4$ GPa.[19] Numerical values are listed in Table IV for all of the alloys.

The structural stiffness of the actual 3D microstructures is compared in Fig. 5, where the solid lines,

[†]Because the reinforcing intermetallic or the whole eutectics are assumed either as a solid ceramic skeleton (AZ91D) or as a long fiber composite (other alloys), microstructural parameters such as grains size are not considered. There would be a grain size effect in the case of the whole eutectics through a Hall–Petch effect associated with the lamellar spacing[25] but only for plastic strains, which are beyond those considered for the current modeling.
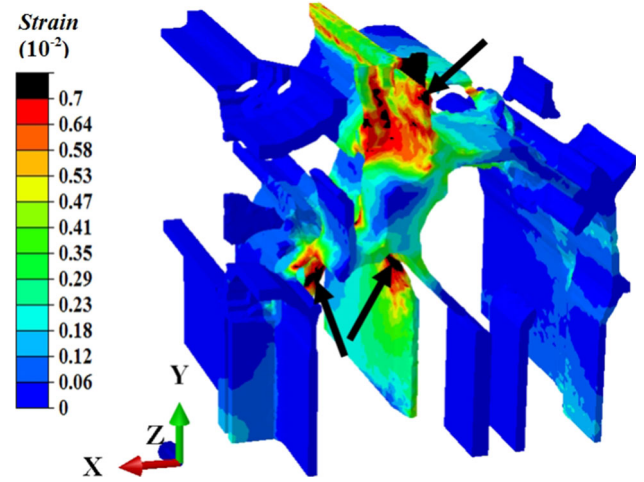

Fig. 3. Distribution of cracked sites, represented by the black regions (a few are arrowed), across the 3D structure of Fig. 1, loaded along the direction Y, after an applied strain of 1%.

with slope E_{3Dp} as per Eq. 3, represent the elastic behavior when no damage by cracking is allowed to occur. The numerical values are summarized in Table V, and the monotonic increase in E_{3Dp} with f_p is evident.

The dot-dashed lines show the cumulative effect of cracking of the intermetallic microtrusses and the onset of plastic deformation of the Mg matrix, both assumed to occur at (local) strains of 0.7% and above. The deviations from linearity, or damage initiation strains ε_{in}, are in the range 0.2% to 0.4%. Such low values indicate that many microtrusses are overloaded and crack very early in the test. The ε_{in} values are listed in Table V.

Comparison with Model Structures

The use of standard structures, such as those illustrated by Table VI, allows using simple functional expressions representing upper and lower bounds to characterize the behavior of complex structures such as the present ones.[26] For the structural elastic modulus, the following expression applies:[25–29]

$$E_{3Dp} = E_p f_p^m \qquad (5)$$

where E_{3Dp}, E_p, f_p, and m represent, respectively, the 3D structural modulus, the constituting phase Young's modulus, the solid phase volume fraction, and a morphology factor (see Table VI).[‡]

[‡]Because the modeling concentrates on the reinforcing by the network, the differences in the alloys chemical composition are reflected only in the elastic constants of the intermetallics, as given by the E_i values in Table IV and are made evident (through Eq. 4) by the slope of the lines through the origin in Fig. 4. There is some effect of E_i (through Eq. 5) on the dispersion-hardening component as well. Solid-solution effects on the overall strength of the alloys are not considered, but it should be kept in mind that they are solute specific and can be quite significant, see for example Ref. 6.

Table III. Dimensions of the sampled volume, the volume fraction of the percolating phase f_p, within the sampled volume and of α-Mg, f^α, and intermetallic f^i within the respective eutectics

Alloy	L (μm)	f_p (%)	f^α (%)	f^i (%)	$f_p \times f^i$ (%)	References
AZ91D (core)	≈ 13.5	5.9	0	100	5.9	8
Mg-3.53 mass% Nd	11.4	7.5	69.9	30.1	2.3	6
MRI230D	11.6	11.4	61.9	38.1	4.3	This work
AZ91D (corner)	≈ 13.4	12.5	0	100	12.5	8
Mg-2.87 mass% Ce	11.4	21.6	44.2	55.8	12.1	7
Mg-3.44 mass% La	11.6	29.9	55.8	44.2	13.2	6

($f_p \times f^i$) is the volume fraction of the intermetallic with the sampled volume. The alloys are sorted as per their respective f_p value.
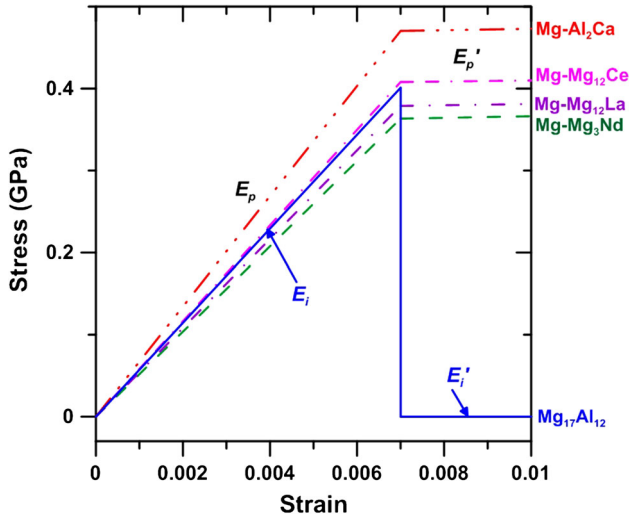

Fig. 4. Stress/strain behavior of the intermetallic (AZ91D alloy, labeled E_i) or the whole eutectics (other alloys, calculated with Eq. 4) assumed for the modeling. The corresponding numeric values are given in Table 4. (For this graph, the materials are all assumed to be long fiber composites.).

With f_p, E_p, and E_{3Dp} values from Tables III, IV, and V, m-values were determined for the current structures and listed in Table V. They consistently approximate 2 for the lower f_p values, as expected for open-cell structures according to the model structures of Table VI, dropping to about 1.65 for 22% and above, suggesting a tendency to mimic long fiber composites ($m \sim 1$).[§]

For fiber composites,[26] the lower and upper limits to the elastic modulus are, respectively, represented by the Reuss' and Voigt's bounds, labeled E_{RB} and E_{VB}:

$$E_{RB} = \frac{E_m E_p}{f_p E_m + (1 - f_p) E_p} = 0 (\text{Reuss' bound}) \quad (6)$$

$$E_{VB} = f_p E_p + (1 - f_p) E_m = f_p E_p (\text{Voigt's bound}) \quad (7)$$

where E_m (=0) represents the open spaces of the 3D percolating networks in Fig. 1.

For foamed solids, bending-dominated and stretch-dominated structures[¶] manifest, respectively, the lower and upper bounds of the structure modulus, denoted by E_{BD} and E_{SD}:

$$E_{BD} = f_p^2 E_p \quad (8)$$

$$E_{SD} = \frac{f_p E_p}{3} \quad (9)$$

To compare E_{VB}, E_{BD}, and E_{SD} for all alloys in a single graph, the three parameters have been normalized by the corresponding E_{VB} value; i.e., Equations 7–9 take the form:

$$E_{VB} = 1 \quad (7a)$$

$$E_{BD} = f_p \quad (8a)$$

$$E_{SD} = \frac{1}{3} \quad (9a)$$

In practice, the normalizing produced a common VB and SD behavior, but because of the stronger dependence on f_p, it differentiated the alloys by their BD behavior.

Equations 6 and 7a–9a, plotted together in Fig. 6, show that the networks with less than 22% in volume fraction closely match the behavior of BD

[§]Recent FEM modeling and experiments by Challis et al.[31] on Ti alloy scaffolds, created using selective laser melting, resulted in stiffness values (see their Fig. 3) that closely match the current alloys' E_{3Dp} values of Table V for comparable volume fractions.

[¶]The Voigt's bound assumes all microtrusses aligned parallel to the stress axis (see diagrams in Table VI). In the SD configuration, only 1/3 of the interconnected branches are loaded in tension, with the rest orientated across the tensile axis. In the BD configuration, loads are transmitted exclusively through elastic bending of the microtrusses.[32]

Table IV. Moduli, E_i (E_i'), E_α (E_α'), and E_p (E_p'), respectively, for the intermetallic, α-Mg, and the percolating phases

Percolating Phase	E_i (GPa)	E_i' (GPa)	E_α (GPa)	E_α' (GPa)	E_p (GPa)	E_p' (GPa)	References
$Mg_{17}Al_{12}$	57.3[20]	0	Not applicable		57.3	0	8
Mg-Mg_3Nd	70.3[21]		44[22]	1.4[19]	51.9	0.98	6
Mg-$CaAl_2$	105.0[23]				67.2	0.87	This work
Mg-$Mg_{12}Ce$	69.6[7]				58.3	0.62	7
Mg-$Mg_{12}La$	66.9[24]				54.1	0.78	6

Primed values (within brackets) correspond to cracking of the intermetallic (E_i') and/or the onset of plastic deformation of the α-Mg (E_α') within the eutectic, past the strain of 0.7%.
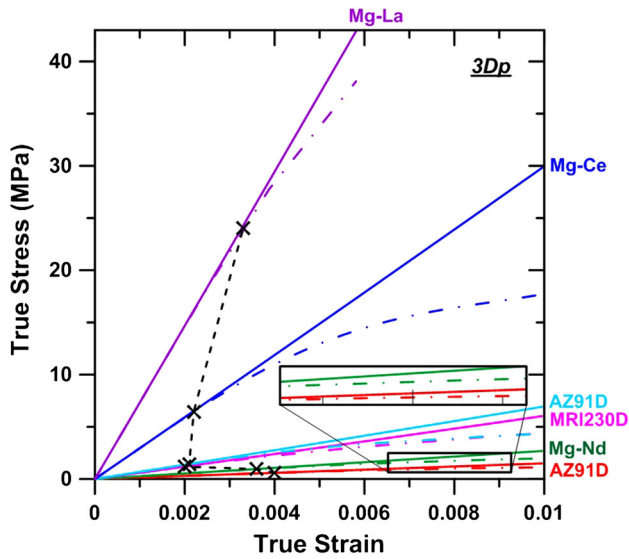

Fig. 5. Stress/strain responses of the 3D percolating networks—the solid and dot-dashed lines correspond, respectively, to purely elastic behavior of the percolating phase and when damage by cracking of the intermetallic is allowed to occur. The crosses (linked by a dashed line) indicate the onset of damage.

structures, whereas the Mg-Mg$_{12}$La network, with 30% of percolating phase, is stiffer than the corresponding SD model structure.

Structural Efficiency and Damage Generation

A hard phase dispersed in a metallic matrix normally increases the latter's elastic modulus and strain-hardening rate in proportion to both the volume fraction and the elastic modulus of the reinforcement.[33] Damage by cracking of reinforcements decreases the intensity of both reinforcing effects[34–37] at large strains. The reinforcing effects of a structurally efficient stretch-dominated ceramic structure, (such as in long fiber unidirectional composites) are the highest of all the configurations but are limited to low strains because of the early fracture of the reinforcement.[6–8] Being very compliant, low-efficiency bending-dominated structures sacrifice the initial stiffening of the composite in favor of a delayed onset of cracking, extending the

reinforcement into the plastic regime of the matrix because of the lower rate of development of damage. With reference to Fig. 6, the stretch-dominated behavior of the Mg-Mg$_{12}$La network is expected to introduce the greatest strengthening of all of the studied microstructures, but at the same time it should have the highest rate of damage development, imposing a limit onto the overall ductility of the composite. By the same token, the opposite is expected for the BD microstructures.[6–8] The widely different rates of damage generation are illustrated by Figs. 3 and 7. The BD microstructure of alloy AZ91 is an example of slow development of damage in comparison with the SD Mg-Mg$_{12}$La network. The MRI230D alloy (Fig. 3) represents an intermediate case. These conclusions regarding relative stiffness and ductility were generally confirmed through short annealing experiments aimed at breaking up the spatial interconnection in HPDC Mg-La and Mg-Nd alloys.[6]

Strengthening Effects

The contribution of the 3D network to the alloy's yield strength has been calculated in detail in earlier studies[6–8] in relation to AZ91, Mg-La, and Mg-Ce alloys. The analysis is extended here to include the MRI230 alloy. The network's contribution to yield strength (i.e., that due exclusively to the spatial interconnection), denoted by σ_{3Dp}, was defined as the stress at 0.6% total strain in the respective stress/strain curves (allowing for damage effects) of Fig. 5, which approximately corresponds to (0.2% off-set) yield point of a dispersion reinforced alloy. The values are shown in Fig. 8.

To calculate the total contribution to the alloy's strength, the dispersion hardening σ_d, i.e., arising from the local interaction of the intermetallic with the deforming Mg matrix in which it is embedded, must be also be considered.[35,36,38]

$$\sigma_d = E_i \times (f_p \times f^i) \times 0.002 \tag{10}$$

with ($f_p \times f^i$) values given in Table II.

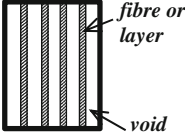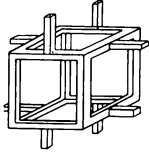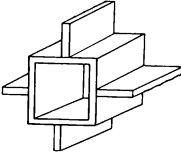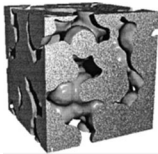The σ_d values are also shown in Fig. 8 (the numerical values are listed in Table VII). The two contributions are roughly of the same order,

Table V. Structural stiffness (E_{3Dp}) of the percolating intermetallic/eutectic networks E_{3Dp} and their respective crack initiation strains ε_{in}, defined by the point where the relevant curves in Fig. 5 differ by 2% in true stress

Alloy	Percolating Network	$f_p(\%)$	E_{3Dp} (MPa)	ε_{in} (%)	m-value	References
AZ91D (core)	$Mg_{17}Al_{12}$ (core)	5.9	149.4	0.40	2.1	8
Mg-3.53mass%Nd	Mg-Mg_3Nd	7.5	269	0.36	2.0	6
MRI230D	Mg-$CaAl_2$	11.4	603.1	0.20	2.2	This work
AZ91D (corner)	$Mg_{17}Al_{12}$ (corner)	12.5	693.1	0.21	2.1	8
Mg-2.87mass%Ce	Mg-$Mg_{12}Ce$	21.6	2987.9	0.22	1.9	7
Mg-3.44mass%La	Mg-$Mg_{12}La$	29.9	7407.8	0.33	1.7	6

The m-values are the morphology factors determined as per Eq. 5.

Table VI. Model structures and their corresponding morphological factors, m

Structure type	Configuration	m-value	Reference(s)
Unidirectional fibrous or multiple-layered structure	*fibre or layer* / *void*	1	26
Open-cell cellular structure		2	27,28
Closed-cell cellular structure		3	
Overlapping solid spheres		4	29,30

especially for the BD structures (i.e., $f_p < 20\%$). The ratio of σ_{3Dp} to the alloy's strength, shown in Table VII, increases monotonically with the volume fraction of percolating phase f_p and is as high as ~30% for the Mg-La alloy. In practical terms, an upper bound to the total contribution to the strength is twice the value given by Eq. 10.
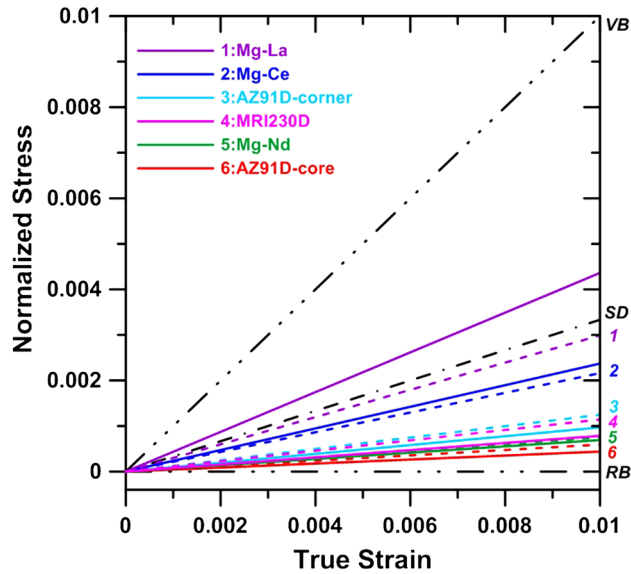
Fig. 6. The solid lines are the normalized stress/strain responses of the 3D percolating networks (3Dp), compared with those of model structures as per Eqs. 6 and 7a–9a, namely: Voigt's bound (VB); stretch-dominated (SD), bending-dominated (BD); and Reuss' bound (RB). The short-dashed lines represent the standard BD behavior as per each alloy's f_p-value, identified by the numerals 1 through 6.
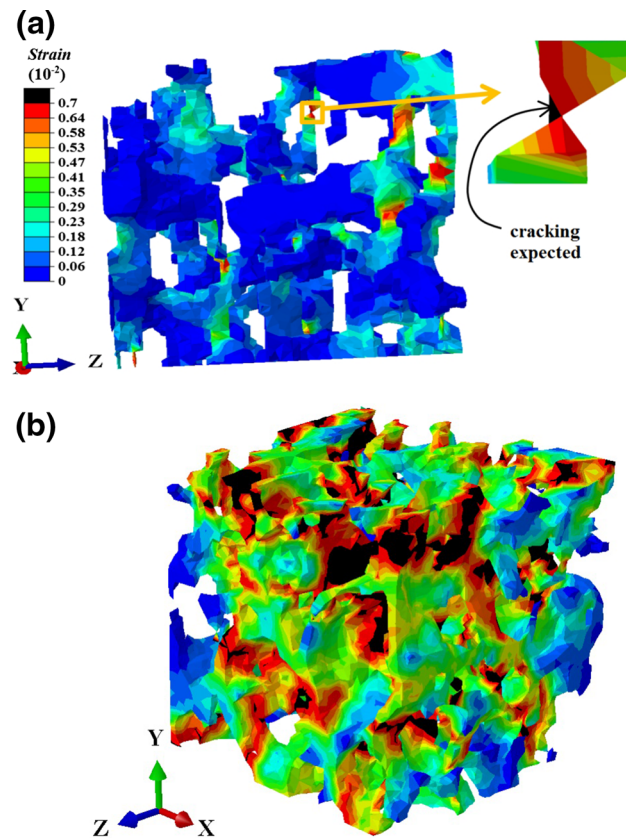

(a)

(b)

Fig. 7. (a) Damage by cracking in the $Mg_{17}Al_{12}$ network in AZ91D (corner) after an applied strain of $\sim$0.2%; the black regions identify local strains higher than 0.7%, and where cracking is expected to occur. (b) Damage in $Mg-Mg_{12}La$ network[6] at an applied strain of 1% (the same as that for the MRI230D network in Fig. 3).
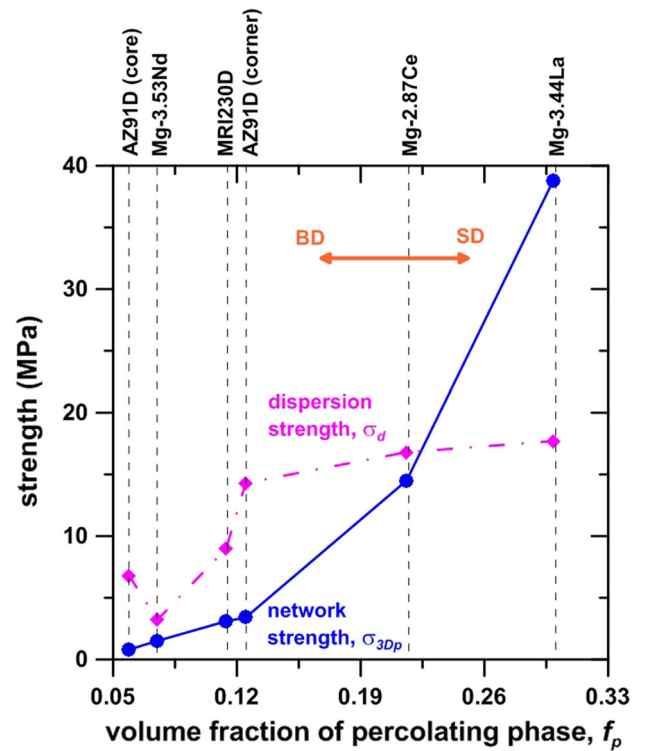

Fig. 8. The strengthening resulting from spatial interconnection σ_{3Dp} and dispersion strengthening σ_d at yield (0.2% off-set strain) for the alloys of Fig. 5.

Table VII. Contributions through the spatial interconnection σ_{3Dp} and dispersion hardening σ_d to the alloys (0.2% off-set) yield strength (YS)

Percolating phase	YS (MPa)	f_p (%)	σ_{3Dp} (MPa)	σ_d (MPa)	σ_{3Dp}/ YS (%)	YS value from
$Mg_{17}Al_{12}$ (core)	103	5.9	0.8	6.8	1	2
$Mg-Mg_3Nd$	127	7.5	1.4	3.2	1	11
$Mg-CaAl_2$	176	11.4	3.1	9.0	2	39
$Mg_{17}Al_{12}$ (corner)	103	12.5	3.4	14.3	3	2
$Mg-Mg_{12}Ce$	136	21.6	14.5	16.8	11	11
$Mg-Mg_{12}La$	141	29.9	36.7	17.7	26	11

CONCLUSIONS

- 3D FIB tomography showed that the squeeze-cast MRI230D alloy developed an interconnected network of the percolating intermetallic/eutectic phases akin to that of cellular solids, morphologically similar to those of HPDC AZ91D, Mg-Nd, Mg-Ce, and Mg-La alloys.
- A comparison of the FE modelled behavior of the 3D interconnected microstructures showed that for volume fractions below 22% the networks can be expected to exhibit bending-dominated deformation

behavior, hence limited initial strengthening of the alloys, but should be less prone to develop damage by cracking of the intermetallic. For volume fractions of 22% and above, the strengthening increases rapidly but the overall ductility can be compromised by profuse early cracking.

- At yield, all networks contribute to the alloy's strength an amount that is comparable with that expected from a similar volume fraction of dispersed particles. The overall (maximum) contribution to the strength stemming from a 3D interconnected network can be estimated as twice the value expected from the dispersion of a similar volume fraction of the percolating phase.

ACKNOWLEDGEMENTS

REFERENCES

1. C.H. Cáceres, W.J. Poole, A.L. Bowles, and C.J. Davidson, *Mater. Sci. Eng. A* 402, 269 (2005).
2. K.V. Yang, A.V. Nagasekhar, C.H. Caceres, and M.A. Easton, *Mater. Sci. Eng. A* 542, 49 (2012).
3. D. Amberger, P. Eisenlohr, and M. Göken, *Acta Mater.* 60, 2277 (2012).
4. B.S. Shin, J.W. Kwon, and D.H. Bae, *Met. Mater. Int.* 15, 203 (2009).
5. A.V. Nagasekhar, C.H. Cáceres, and C. Kong, *Mater. Charact.* 61, 1035 (2010).
6. B. Zhang, S. Gavras, A.V. Nagasekhar, C.H. Caceres, and M.A. Easton, *Metall. Mater. Trans. A* 45, 4386 (2014).
7. B. Zhang, A.V. Nagasekhar, X. Tao, Y. Ouyang, C.H. Caceres, and M. Easton, *Mater. Sci. Eng. A* 599, 204 (2014).
8. B. Zhang, A.V. Nagasekhar, T. Sivarupan, and C.H. Caceres, *Adv. Eng. Mater.* 15, 1059 (2013).
9. A.V. Nagasekhar, C.H. Cáceres, and C. Kong, *J. Phys.: Conf. Series* 240 (2010).
10. A.V. Nagasekhar, M.A. Easton, and C.H. Cáceres, *Adv. Eng. Mater.* 11, 912 (2009).
11. T.L. Chia, M.A. Easton, S.M. Zhu, M.A. Gibson, N. Birbilis, and J.F. Nie, *Intermetallics* 17, 481 (2009).
12. Y. Terada, N. Ishimatsu, Y. Mori, and T. Sato, *Mater. Trans. (JIM)* 46, 145 (2005).
13. B. Cantor and G.A. Chadwick, *J. Mater. Sci.* 10, 578 (1975).
14. M. Sahoo and R.W. Smith, *Metal Sci.* 9, 217 (1975).
15. D. Stalling, M. Westerhoff, and H.-C. Hege, *Visualization and Mathematics* (Berlin: Springer, 1997).
16. K. Ozturk, Y. Zhong, A.A. Luo, and Z. Liu, *JOM* 40 (2003).
17. O.C. Zienkiewicz and R.L. Taylor, *The Finite Element Method* (Columbus: McGraw-Hill Book Company, 1989).
18. D. Hull, *An Introduction to Composite Materials* (Cambridge: Cambridge University Press, 1981).
19. C.H. Cáceres and P. Lukác, *Phil. Mag. A* 88, 977 (2008).
20. N. Wang, Y. Wei-Yang, B.-Y. Tang, L.-M. Peng, and W.-J. Ding, *J. Phys. D* 41, 195408 (2008).
21. H. Zhang and S. Wang, *Acta Metall. Sinica* 48, 889 (2012).
22. T. Sumitomo, C.H. Cáceres, and M. Veidt, *J. Light Metals* 2, 49 (2002).
23. H. Anton and P.C. Schmidt, *Intermetallics* 5, 449 (1997).
24. J. Wrobel, L.G. HectorJr, W. Wolf, S.L. Shang, Z.K. Liu, and K.J. Kurzydlowski, *J. Alloy Compd.* 512, 296 (2012).
25. R.W. Armstrong, *The Yield and Flow Stress Dependence on Polycrystal Grain Size*, ed. T.N. Baker (London: Applied Science Publishers, 1983), pp. 1–31.
26. M.F. Ashby and Y.J.M. Brechet, *Acta Mater.* 51, 5801 (2003).
27. L.J. Gibson and M.F. Ashby, *Proc. R. Soc. Lond. A* 382, 43 (1982).
28. S.K. Maiti, L.J. Gibson, and M.F. Ashby, *Acta Metall.* 32, 1963 (1984).
29. G. Bruno, A.M. Efremov, A.N. Levandovskyi, and B. Clausen, *J. Mater. Sci.* 46, 161 (2011).
30. A.P. Roberts and E.J. Garboczi, *J. Am. Ceram. Soc.* 83, 3041 (2000).
31. V.J. Challis, X. Xu, L.C. Zhang, A.P. Roberts, J.F. Grotowski, and T.B. Sercombe, *Mater. Des.* 63, 783 (2014).
32. V.S. Deshpande, M.F. Ashby, and N.A. Fleck, *Acta Mater.* 49, 1035 (2001).
33. C.H. Cáceres, J.R. Griffiths, and P. Reiner, *Acta Mater.* 44, 15 (1996).
34. C.H. Cáceres, *Alum. Trans.* 1, 1 (1999).
35. Y. Brechet, J.D. Embury, S. Tao, and L. Luo, *Acta Metall. Mater.* 39, 1781 (1991).
36. C.H. Cáceres and J.R. Griffiths, *Acta Mater.* 44, 25 (1996).
37. P.J. Withers, W.M. Stobbs, and O.B. Pedersen, *Acta Metall.* 37, 3061 (1989).
38. L.M. Brown and W.M. Stobbs, *Phil. Mag.* 23, 1185 (1971).
39. H.E. Friedrich and B.L. Mordike, *Magnesium Technology: Metallurgy, Design Data, Automotive Applications* (New York: Springer, 2006).